Characterization of Packed Bed Reactors Using X-Ray Microtomography: Effect of Particle Irregularity and Particle Size Distribution on the Bed Morphology

Zahra Ghasemi Monfared*, Gunnar Hellström*, Ryan Robinson and Kentaro Umeki***

zahgha@ltu.se

* Department of Engineering Sciences and Mathematics, Luleå University of Technology, 971 87 Luleå, Sweden

** Höganäs AB, Bruksgatan 35, 263 39 Höganäs, Sweden

Abstract

Packed bed reactors (PBRs) have been widely utilized in chemical and process industries in a variety of particle-based applications, from catalytic reactors and metallurgical furnaces to gasifiers and energy storage systems. Flows and heat and mass transfer through PBRs, as well as the progress of the chemical process, are strongly influenced by randomly filled beds of particles.

It is thus crucial to have a detailed understanding of the packed bed structure and its physical and thermophysical properties in order to design PBR accurately. Recently, many studies utilized numerical modeling, as well as advanced imaging techniques, to improve the understanding of porous bed structure and its effects.

One of the research gaps in the literature is how the irregularity of particle shapes and particle size distributions affect the particle packing and effective transport parameters such as thermal conductivity and mass diffusivity. This study investigates the above issues by X-ray microtomography (XMT) imaging.

Using XMT imaging, it is possible to analyze the structure of packed beds and extract its morphological properties, such as void fraction and tortuosity to highlight the influence of particle size and particle size distribution on them.

1. Introduction

Packed bed reactors (PBRs), also known as fixed bed reactors, find numerous applications in the chemical and process industries for a wide range of particle-based applications, including catalytic reactions, gasifiers, metallurgical furnaces and cooling and energy systems. PBRs consist of beds randomly filled with particles [1]. Permeability is one of the important parameters of the porous media that describes the inverse of the resistance for fluid to flow through porous media [2]. According to Kozeny equation [3] the permeability of the porous medium is defined as,

$$k = \frac{\Phi_s^2 d_p^2}{180} \frac{\epsilon^3}{(1-\epsilon)^2}, \quad \text{Eq. 1}$$

where k is the permeability, ε is the bed void fraction and $\Phi_s$is the sphericity of the particles. Furthermore, the diffusion of fluid within the pores of a packed bed could be defined as [4]

$$\frac{1}{D_{eff}} = \frac{\epsilon}{\tau}\left(\frac{1}{D_A} + \frac{1}{D_{Kn}}\right), \quad \text{Eq. 2}$$

where D_{eff} is the effective diffusivity, τ is the tortuosity of fluid flow within the gaps between the particles, D_A is the molecular diffusivity of gas A in the mixture and D_{Kn} is its Knudsen diffusivity.

As Eq. 1 and 2 suggest, it is important to obtain a detailed understanding of the packed bed morphology, i.e. the void fraction and tortuosity.

Void fraction is a fundamental porous medium characteristic that is defined as the fraction of the void between the particles to the total volume of the packed bed. The bed void fraction is highly dependent on the shape, size and packing arrangement of the particles. The viable void fractions of the ordered packing of monodispersed spherical particles range from 0.26 to 0.46; whereas disordered packings, polydispersed particles and irregular-shaped particles exhibit a wider range of bed void fractions [5].

The other parameter is tortuosity that correlates with how curvy or twisted flow paths are in a porous material. It is defined as the ratio of the actual length of the path through the pores to the shortest straight-line distance between two points. In numerous practical scenarios, tortuosity could be assumed to be affected by the morphology of the pore network structure [6–8].

In different disciplines, the definitions of tortuosity can be broadly categorized into four types, namely, geometrical, electrical, diffusive and hydraulic [7]. This study specifically concentrates on geometrical tortuosity conventionally defined as the ratio of the actual length passed by fluid within the porous structure to the shortest length in absence of particles. The geometrical tortuosity has been predicted and analyzed by different theoretical attempts, such as lattice percolation theory [8] or a combination of the continuum percolation model with fractal theory in media with diverse geometric shapes [9,10]. Moreover, there are variety of popular empirical correlations for estimation of tortuosity within packed beds. These correlations date back to 1873 where Maxwell proposed a correlation for electrical tortuosity within a porous medium all the way to the recent years that the scientists tried to develop tortuosity equations that could cover a wide range of packed beds [3,11–19]. These correlations mainly give tortuosity as a function of the bed void fraction and are developed for monodispersed spherical packed beds and their accuracy for polydispersed and irregular particle packings is not known. Moreover, studies on the geometrical tortuosity within complex porous structures surrounding non-spherical particles with high packing fractions remain scarce. Consequently, a comprehensive understanding of the impact of non-spherical particle characteristics, such as shape, size and size distribution on pore space tortuosity is still lacking.

One of the approaches estimating the tortuosity of packed beds is Pore Network Model (PNM). The PNM has emerged as a simple and efficient methodology for simulating transport within porous materials [20–26]. Unlike the prevalent continuum modeling, which treats porous materials as volume-averaged continua without resolving microscale intricacies, PNM offers an alternative approach and treats the pore space within the packed bed as a network of interconnected channels. The graph theory is used to analyze the flow paths and calculate tortuosity [27].

Experimentally, X-Ray Micro-Tomography (XMT) is a very useful tool for imaging and analyzing the details of the porous structure of packed beds [28,29]. With advancements in computational power and development of efficient algorithms, powerful tools have emerged to process three-dimensional images obtained by XMT. For instance, Cooper et al. [30] and Al-Raoush et al. [31] proposed different open-source algorithms for obtaining tortuosity from tomographic data.

In this study, tortuosity and void fraction of packed beds consisting of irregular-shaped particles with narrow and wider particle size distribution have been investigated using XMT-based images. The void fractions of the packed beds have been compared with each other and with theoretical values obtained from BCC (Body-Centered Cubic) and FCC (Face-Centered Cubic) packings of mono-sized spherical particles. Tortuosity has been computed using PNM approach in DRAGONFLY® software and the tortuosity distribution within the packed beds have been compared with the empirical data used in the literature. The specific focus of this study is the influence of particles size and particle size distribution on the void fraction and tortuosity distribution.

2. Methodology

2.1. Geometry and Material Properties

The packed beds used in this study have been generated in cylindrical containers with diameter of 21 mm and height of 23 mm. Six different samples with different particle sizes ranging from 180 µm to 6.3 mm with different distributions have been employed in this work. The sample names starting with MDP are monodispersed particles and the ones starting with PDP indicate the samples with polydispersed particles. This variety can exhibit the influence of particle size and size distribution on the bed morphology. The information regarding minimum, and maximum particle diameters of each sample as well as the mean and standard deviation of the log-normal distribution have been mentioned in Table 1.

Table 1. Particle size distribution characteristics of the samples used in this study.

Sample Name	Dmin [mm]	Dmax [mm]	Mean [mm]	Log-Normal Standard Deviation [-]
MDP1	0.315	0.4	0.357	0.021
MDP2	2	3.15	2.575	0.575
MDP3	4	6.3	5.15	0.321

The material used for the packed beds is densified biochar obtained from dried spruce chips (including bark) with envelope density of 783 kg/m3. The conditions of the biochar production as well as sieving process have been mentioned in [32].

2.2. Image acquisition using X-Ray Micro-Tomography (XMT)

In order to get the structure of the packed beds, the samples have been prepared as shown in **Error! Reference source not found.**.

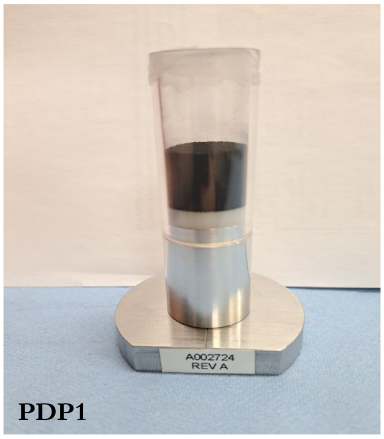

Figure 1. The packed bed of sample PDP1 prepared in the sample holder for being inserted into the XMT device.

Then the samples were inserted into the XMT device, i.e. a Zeiss Xradia 510 Versa. Shortly put, the material in the XMT is exposed to an X-ray beam that will be either absorbed or diffracted or transmitted through the material (Wildenschild and Sheppard, 2013) [33]. Then the transmitted radiation with lower intensity due to passing through the sample, is received by the detectors.

Depending on the particle size distribution, the scanning has been performed with an X-ray tube voltage in the range of 40 kV and to minimize beam hardening artifacts, a 3W tube power utilizing an LE1 or LE2 X-ray filter (depending on the sample features) has been used.

For each scan, 1601 projections have been collected through a full 360˚ rotation to minimize reconstruction artifacts. The images have been obtained with different resolutions and acquisition times based on the feature size of each sample. The resolutions for MDP1 and PDP2 with smallest particle sized equal to 0.315mm and 0.18mm, respectively, has been selected to be 5µm and for the rest of the samples 22 µm has been chosen as resolution.

The raw data is exported into DRAGONFLY® software (Version 2022.2 Build 1367). This process produced a stack of 16-bit TIFF images. Figure 2 displays an example of X-ray raw grayscale image of the horizontal plane from the sample MDP2.

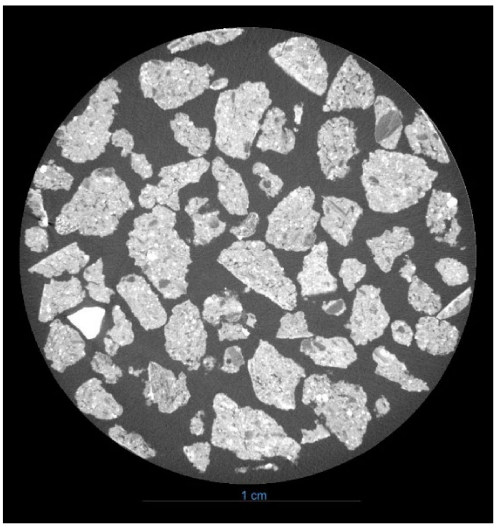

Figure 2. An example of the raw grayscale image obtained from the XMT for MDP2.

Figure 2 depicts that the XMT settings have adequately boldened the interface area between the biochar particles and the void space.

Subsequently, each stack of grayscale images should undergo segmentation process where the particles could be separated from the pore space and then by stacking the binarized images, a 3D

representation of the pore space structure would be obtained. To achieve accurate results for separating the two distinct phases (the particles and the void space), a thresholding method has been employed, involving manual interaction for the selection of peaks from the bimodal histogram of grayscale intensity values. The respective phases were characterized by their grayscale appearance, which corresponds to X-ray attenuation and, in turn, reflects the density variations of different phases within the samples.

2.3. Calculation of Void Fraction

2.3.1. Theoretical Values for the Void Fraction of Particle Packings

One of the key parameters for characterizing the packed bed morphology is the bed void fraction, which is expressed as the fraction of the volume of void space between the particles over the total volume of the packed bed. Sphere packing is a fundamental concept for understanding the arrangement of particles within a given space. Theoretical studies of sphere packing involve the investigation of different configurations, such as face-centered cubic (FCC), body-centered cubic (BCC), and hexagonal close-packed (HCP) arrangements. Each packing arrangement exhibits distinct void spaces between the spheres. For instance, the FCC, characterized by spheres positioned at the vertices of a cube and on the faces, and the HCP, where spheres form a double layer with an offset, both exhibit the maximum possible packing fraction for spherical particles resulting in void fraction of 0.26. Moreover, BCC configuration yields void fraction of 0.32. The abovementioned values of void fraction are theoretical and defined for arrangements of mono-sized spherical particles. These values are used as benchmarks for the comparison with the results obtained by the XMT analyses.

2.3.2. Calculation of Void Fraction from XMT-Based Images

For extracting the void fraction from the XMT images, the slice analysis in DRAGONFLY® has been carried out for the vertical slices that are in fact cross section planes parallel to the bottom of the bed. A schematic of the segmented image from the same slice of MDP2 as in Figure 2 has been displayed in Figure 3. The yellow regions in Figure 3 are the void and the black spots are the particles binarized in the segmentation process.

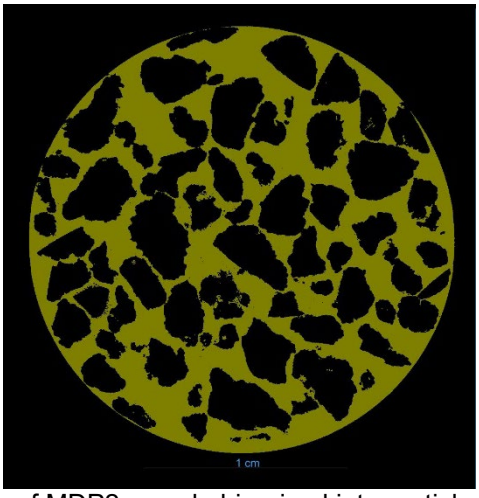

Figure 3. The segmented image of MDP2 sample binarized into particles and void space between.

The area-averaged void fraction for each section is then calculated as below:

$$\bar{\varepsilon}_{section} = \frac{A_{void}}{A_{section}}, \qquad \text{Eq. 3}$$

where A_{void} is the area of void space in each section and $A_{section}$ is the area of each circular section. A_{void} can be extracted from slice analysis in DRGONFLY® for slices with longitudinal intervals depending on the resolutions mentioned in table 2. Then, the area-based void fractions have been averaged out for all sections to obtain the overall bed void fraction for each sample.

2.4. Calculation of Tortuosity

2.4.1. Tortuosity Based on Empirical Correlations

Variety of empirical correlations have been proposed in the literature for estimating tortuosity within packed beds. Some of these correlations together with their applicable void fraction range are summarized in Table 2. Most of these correlations are derived for spherical particles and from experiments, such as diffusivity or conductivity measurements.

Table 2. List of empirical formulas for calculating tortuosity in packed beds of spherical particles

Model Name	Correlation	Applicable void fraction range
Maxwell (1873) [11]	$\frac{3}{2}-\frac{1}{2}\varepsilon$	Not specified
Bartell & Osterhof (1928) [12]	$\frac{\pi}{2}$	$\varepsilon = 0.4$
Carman (1937) [3]	$\sqrt{2}$	$\varepsilon = 0.4$
Weissberg (1963) [13]	$1-\frac{\ln(\varepsilon)}{2}$	$0.36 < \varepsilon < 1$
Bear (1972) [14]	$\frac{1}{\varepsilon^{0.4}}$	Not specified
Comiti & Renaut (1989) [15]	$1-0.41\ln(\varepsilon)$	Not specified
Du Plessis & Masliyah (1991) [16]	$\frac{\varepsilon}{1-\sqrt[3]{(1-\varepsilon)^2}}$	Not specified
Iversen & Jorgensen (1993) [17]	$\sqrt{1+2(1-\varepsilon)}$	$0.4 < \varepsilon < 0.9$
Boudreau (1996) [18]	$\sqrt{1-ln(\varepsilon^2)}$	Not specified
Ahmadi et al. (2011) [19]	$\sqrt{\frac{2\varepsilon}{3[1-1.108(1-\varepsilon)^{\frac{2}{3}}]}+\frac{1}{3}}$	$\varepsilon > 0.4$

As could be understood from Table 3, the tortuosity correlations have different mathematical forms and there are inconsistencies between the values obtained. In this study, the computed tortuosity values from XMT images have been compared to the ones from the most common models applicable to the present case and then the method has been used to investigate the influence of PSD on tortuosity of packed beds.

2.4.2. Calculation of Tortuosity Based on the Pore Network Model (PNM)

Having the 3D pore structure of the packed bed from the XMT data, one could extract the statistical information on the tortuosity of the packed bed. In this regard, the Pore Network Model (PNM) has been employed. PNM involves discretizing the porous structure into interconnected pores and throats, forming a network that represents the material pore-scale geometry and the OpenPNM package in DRAGONFLY® offers a versatile and user-friendly toolset for implementing it (See [27] for additional information about the algorithm).

A schematic of the pore-throat network within MDP2 sample is demonstrated in Figure 4. The bottom half is the 3D image of the packed bed and the top half display the network of pore-throat extracted from the pore structure, it could be seen that the diameter of pores lies between 0.01 and 2.85 mm and the length of the channels are in mostly below 0.35 mm except for the areas closer to the walls where the values are larger up to around 3.45 mm.

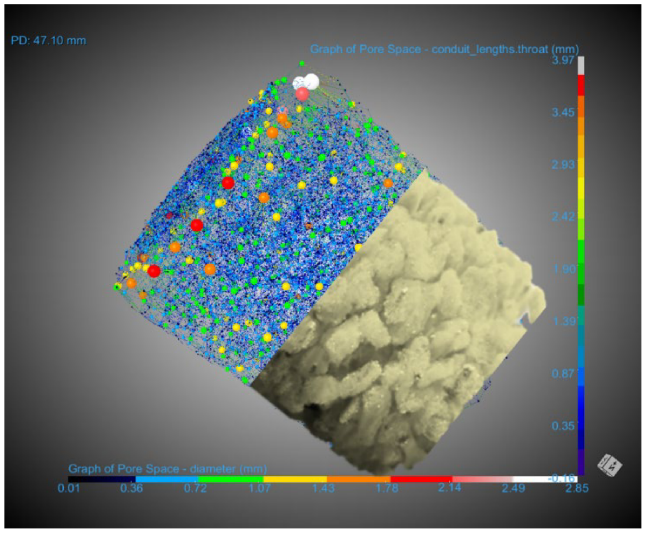

Figure 4. Schematic of the pore-throat network extracted from the pore structure of MDP2 sample.

After the pore-throat network is obtained, all possible tortuous pathways have been analyzed under the restriction that the flow direction would be aligned with the height of the cylinder dictating the inlet as the bottom of the holder and the outlet as the top. The outcome is a histogram of tortuosity values computed through almost all possible ways from inlet and outlet. An example of the outcome of the OpenPNM model for MDP2 is displayed in Figure 5. The top image of Figure 5 depicts the histogram of the tortuosity values distribution. As for the sample MDP2, the smallest values could be related to the passages that are the easiest for the fluid to flow at the regions near the walls. The largest values in the histogram show the longest possible connections from the inlet to the outlet which contribute to the average tortuosity of the bed but might be physically impossible for the fluid to pass through, depending on the throat diameter and channel lengths. The bottom picture in Figure 5 shows the box chart of the tortuosity distribution for MDP2. In the box chart shown, the left most line represents the minimum tortuosity observed in the dataset, which is 1.03. Following that is the left side of the rectangle representing the first quartile of the data (more than 25% of the tortuosity values in the domain and lower than 75% of them), the middle line representing the median and the right side of the rectangle representing the third quartile (larger than 75% of the data and smaller than the remaining 25%). Finally, the left most line is the maximum value of tortuosity (here about 1.18).

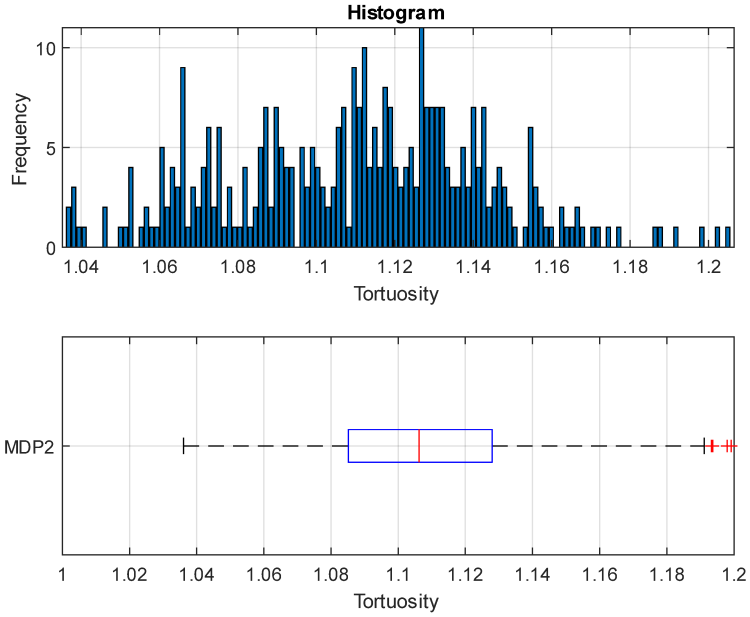

Figure 5. The histogram of the tortuosity values in the MDP2 packed bed from inlet to the outlet (Top) and the box chart related to the tortuosity values (Bottom)

3. Results and Discussions

3.1. Void Fraction

3.1.1. Monodispersed Samples

The void fraction of packed bed depends on the particles shape, size and size distribution. Figure 6 shows the dependency of void fraction to size using the three samples MDP1, MDP2 and MDP3 (with size specifications mentioned in Table 1). As the particles became larger (from average size of 0.575 mm in MDP1 to 5.15 mm in MDP3) the void fraction increased, and the values became further from the maximum theoretical value of tight packing (0.32) for mono-sized spherical packings in BCC arrangements. One reason for this deviation is the irregularity in shape of particles and the deviation from spherical shape as shown in Figure 2. Another reason for the deviation from theoretical values is that the monodispersed distribution of particles in practice introduces a small range of size distribution where smaller particles could fill the gap between slightly larger ones and this could lead to deviation from the theoretical values, as per log-normal distribution characteristics mentioned in Table 1. In other words, MDP1 with the lowest log-normal standard deviation has the lowest void fraction, respectively.

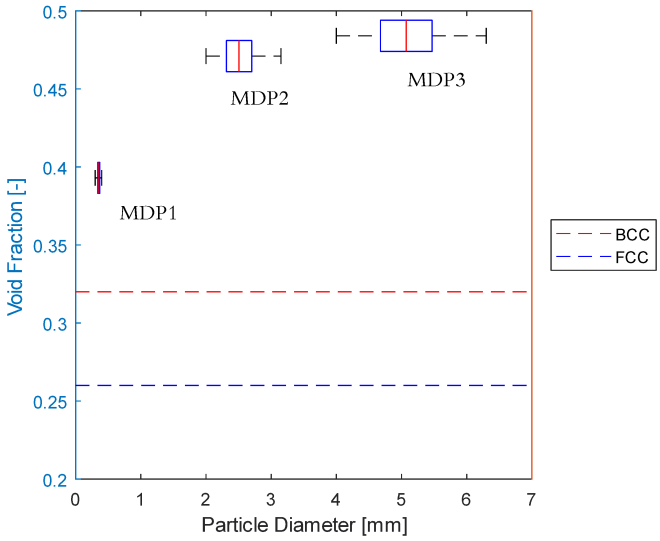

Figure 6. Comparison between the void fraction in samples MDP1, MDP2 and MDP3 as well as the void fractions obtained from theoretical values of packing arrangements of BCC and FCC

3.1.2. Polydispersed Samples

As shown in Figure 7, PDP1 and PDP2 could exhibit smaller volume-averaged void fractions than the minimum theoretical value related to FCC packing. This is because smaller particles (0.18 mm) fits the spaces between larger particles (3 mm for PDP1 and 5mm for PDP2) and reduces the void fraction compared to the case when all particles are mono-sized. On the other hand, in case of PDP3 with smaller value of log normal standard deviation, the majority of particles are in the same size and there are statistically not many small particles to fill the gap between other larger particles. Therefore, the value of void fraction was similar to the values for monodispersed packings (0.47 for PDP3). This could also mean that standard deviation is a better criterion to assess the void fraction distribution within packed beds of particles.

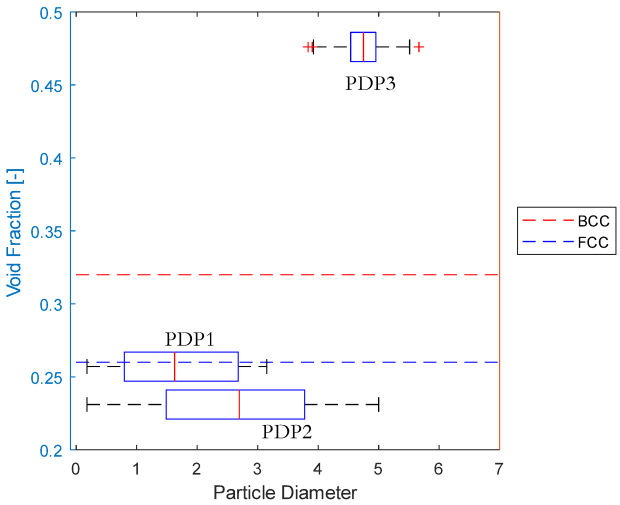

Figure 7. Comparison between the void fraction in samples PDP1, PDP2 and PDP3 as well as the void fractions obtained from theoretical values of packing arrangements of BCC and FCC

3.2. Tortuosity Distribution

3.2.1. Monodispersed Samples

As mentioned in section 2.4.1, the tortuosity in packed beds is not a single value, but a range of values obtained from calculating all the possible paths that a fluid could pass through the void between particles. This tortuosity distribution could give valuable information about the structure of the pore space within the packed beds. Figure 8 shows the distribution for the monodispersed samples. The tortuosity is larger for MDP1, which consists of small particles with narrow size ranges where the fluid cannot pass

through the channels between the particles as easily. Moreover, the distribution of tortuosity is wider, which could be because of the difference between hardship of the fluid to pass through the small particles in the bulk of the packed bed and the possible channels adjacent to the walls.

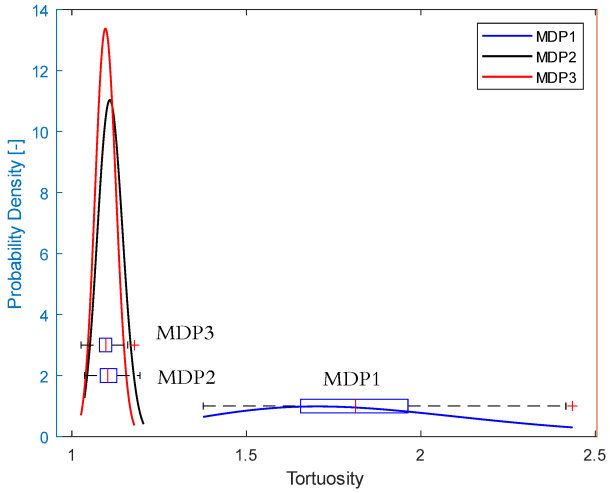

Figure 8. Log-normal distribution of the tortuosity within monodispersed samples visually compared with the box chart of tortuosity distribution.

As mentioned in section 2.4.1, a variety of empirical correlations exist in the literature for tortuosity in packed beds. Figure 9 compares these models with the distribution span of tortuosity obtained from PNM approach for XMT-based images. As mentioned before, the existing empirical models may not be accurate for non-spherical particles as well as beds with wide ranges of PSD. As shown in the figure, the whole range of tortuosity distribution for samples MDP2 and MDP3 fall below the values predicted by the empirical models. Tortuosity distribution of MDP1 is close to the one predicted by the Boudreau model.

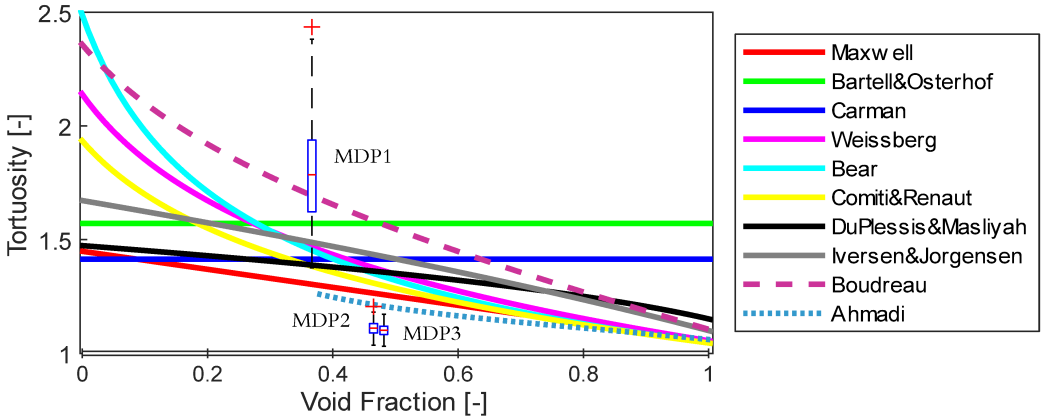

Figure 9. The empirical correlations of tortuosity mentioned in table against bed void fraction and compared with the tortuosity distribution obtained from PNM approach for XMT-based images of the monodispersed samples.

3.2.2. Polydispersed Samples

When it comes to wider ranges of PSD, the tortuosity distribution throughout the porous packed bed has no clear correlation with the void fraction or log-normal standard deviation of particle size distribution. The tortuosity distribution of three polydispersed samples (PDP1, PDP2 and PDP3) have been compared in Figure 10 and Figure 11.

As could be seen in Figure 10, PDP2 and PDP3 predicts close ranges of tortuosity distribution, unlike different values of void fractions and PSD. PDP1 (with PSD range of 0.18 mm to 3.15 mm) displays larger values of tortuosity as well as a wider span for tortuosity distribution. Thereby, no meaningful correlation could be observed between the tortuosity of PDP samples with their respective void fraction or even the log-normal standard deviation of their particle size. One assumption here is that in case of

these polydispersed samples, increasing the maximum diameter of the particles affects the tortuosity distribution and leads to a decrease in the tortuosity values.

Figure 11 shows the difference in tortuosity distributions of the polydispersed samples compared to the empirical models giving tortuosity values based on void fraction. As could be observed, for PDP2 and PDP3 the empirical models have overestimated the values of tortuosity; however, for PDP1 with a wide range of tortuosity distribution, the average could be estimated by Boudreau model, while the minimum value is close to the Bear model prediction. As expected, in wide ranges of PSD, the empirical models cannot completely predict the tortuosity of the packed beds.

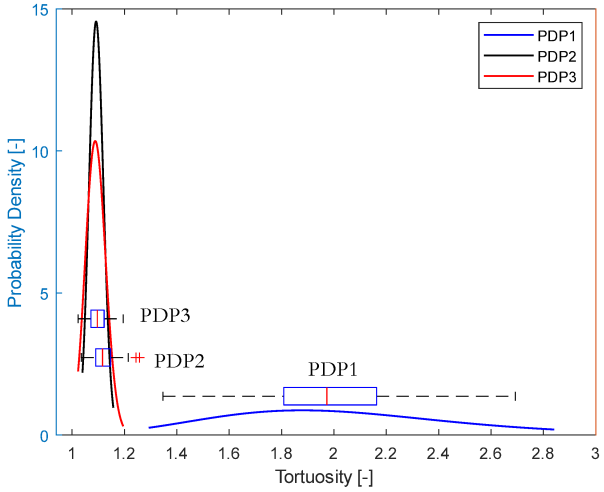

Figure 10. Log-normal distribution of the tortuosity within polydispersed samples visually compared with the box chart of tortuosity distribution.

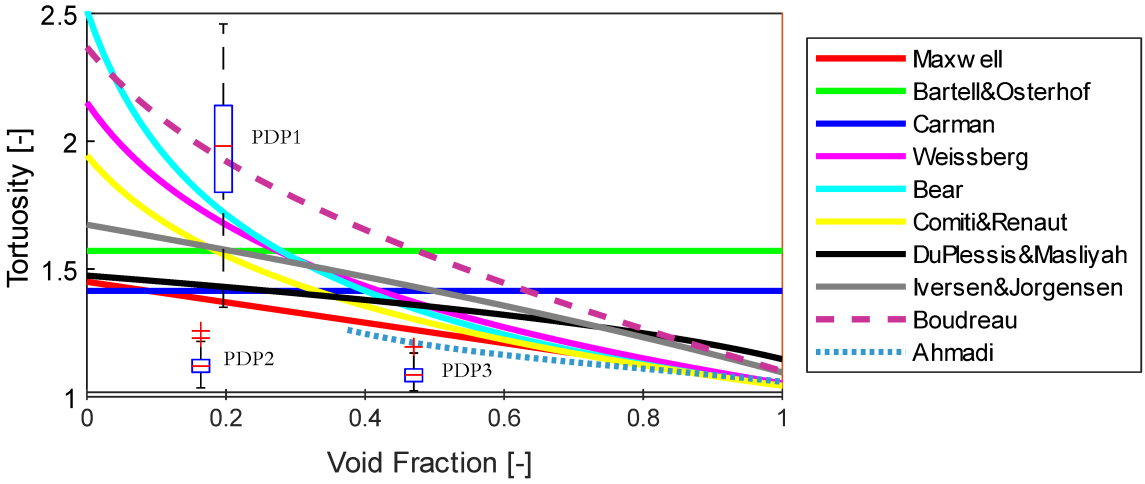

Figure 11. The empirical correlations of tortuosity mentioned in table against bed void fraction and compared with the tortuosity distribution obtained from PNM approach for XMT-based images of the polydispersed samples.

4. Summary

Results of this study demonstrate the significant impact of particle size and particle size distribution on packed bed void fraction and tortuosity for both monodispersed and polydispersed packed beds. When examining the effect of particle size within the monodispersed samples an increase in particle diameter leads to an elevation in void fraction. This increase in void fraction deviates from the theoretical maximum value associated with mono-sized spherical packing in BCC arrangement. This deviation can be attributed to the irregular shape of particles and the departure from a perfect spherical shape. Additionally, the study found that the log-normal standard deviation of particle size within monodispersed samples plays a crucial role in determining void fraction, with lower log-normal standard deviations associated with higher void fractions. Furthermore, it was shown that tortuosity is a function of void fraction particularly in monodispersed samples. Decreasing void fraction leads to an increase of

tortuosity; however, only for the case with smaller log-normal standard deviation, the tortuosity is close to the one predicted by the Boudreau model for spherical particle shapes and for other cases the models overestimate the tortuosity.

In contrast, when exploring polydispersed samples, it was observed that the relationship between particle size, void fraction and tortuosity becomes more complex. Polydispersed particles with low log-normal standard deviation have similar values of void fraction distribution in packed beds as monodispersed particles. However, for a higher log-normal standard deviation, smaller particles within polydispersed samples were found to fill the spaces between larger particles, resulting in a reduced void fraction compared to a scenario with all particles being monosized and arranged in an FCC packing. Moreover, no meaningful correlation has been found between the tortuosity of PDP samples and their respective void fraction or even the log-normal standard deviation of their particle size.

5. Acknowledgements

We thank Mr. Henrik Lycksam, the senior research engineer, and Dr. Fredrik Forsberg, the senior lecturer and head of XMT lab, from Fluid and Experimental Mechanics division of Luleå University of Technology for their contribution with the image acquisition from the X-ray micro-tomography. This study would not be possible without their expertise in taking high quality XMT images.

References

1. Yang, J.; Wang, J.; Bu, S.; Zeng, M.; Wang, Q.; Nakayama, A. Experimental analysis of forced convective heat transfer in novel structured packed beds of particles. *Chem. Eng. Sci.* **2012**, *71*, 126–137, doi:10.1016/j.ces.2011.12.005.
2. Sirimark, P.; Lukyanov, A. V.; Pryer, T. Surface Permeability of Particulate Porous Media. *Transp. Porous Media* **2019**, *130*, 637–654, doi:10.1007/s11242-019-01332-9.
3. Carman, P.G. Fluid flow through granular beds. *Trans. Inst. Chem. Eng* **1937**, *75*, 150, doi:10.1016/s0263-8762(97)80003-2.
4. EUROKIN spreadsheet on requirements for measurement of intrinsic kinetics in the gas-solid fixed-bed reactor Available online: https://eurokin.org/wp-content/uploads/downloads/2019/08/EUROKIN_fixed-bed_html_guide.pdf.
5. Zhang, W.; Thompson, K.E.; Reed, A.H.; Beenken, L. Relationship between packing structure and porosity in fixed beds of equilateral cylindrical particles. *Chem. Eng. Sci.* **2006**, *61*, 8060–8074, doi:10.1016/j.ces.2006.09.036.
6. Punčochář, M.; Drahoš, J. The tortuosity concept in fixed and fluidized bed. *Chem. Eng. Sci.* **1993**, *48*, 2173–2175, doi:10.1016/0009-2509(93)80092-5.
7. Ghanbarian, B.; Hunt, A.G.; Ewing, R.P.; Sahimi, M. Tortuosity in Porous Media: A Critical Review. *Soil Sci. Soc. Am. J.* **2013**, *77*, 1461–1477, doi:10.2136/sssaj2012.0435.
8. Ghanbarian, B.; Hunt, A.G.; Sahimi, M.; Ewing, R.P.; Skinner, T.E. Percolation Theory Generates a Physically Based Description of Tortuosity in Saturated and Unsaturated Porous Media. *Soil Sci. Soc. Am. J.* **2013**, *77*, 1920–1929, doi:10.2136/sssaj2013.01.0089.
9. Xu, W.; Jia, M.; Gong, Z. Thermal conductivity and tortuosity of porous composites considering percolation of porous network: From spherical to polyhedral pores. *Compos. Sci. Technol.* **2018**, *167*, 134–140, doi:10.1016/j.compscitech.2018.07.038.
10. Xu, W.; Jiao, Y. Theoretical framework for percolation threshold, tortuosity and transport properties of porous materials containing 3D non-spherical pores. *Int. J. Eng. Sci.* **2019**, *134*, 31–46, doi:10.1016/j.ijengsci.2018.10.004.
11. Maxwell, J.C. A treatise on electricity and magnetism. *Clarendon Press. London* **1873**, *1*.
12. Bartell, F.E.; Osterhof, H.J. The pore size of compressed carbon and silica membranes. *J. Phys. Chem* **1928**, *32*, 1553.
13. Weissberg, H.L. Effective Diffusion Coefficient in Porous Media. *J. Appl. Phys.* **1963**, *34*, 2636–2639, doi:10.1063/1.1729783.
14. Bear, J. *Dynamics of fluids in porous media*; New York: Elsevier, 1972;
15. Comiti, J.; Renaud, M. A new model for determining mean structure parameters of fixed beds from pressure drop measurements: application to beds packed with parallelepipedal particles. *Chem. Eng. Sci.* **1989**, *44*, 1539–1545, doi:10.1016/0009-2509(89)80031-4.
16. Du Plessis, J.P.; Masliyah, J.H. Flow through isotropic granular porous media. *Transp. Porous Media* **1991**, *6*, 207–221, doi:10.1007/BF00208950.
17. Iversen, N.; Jørgensen, B.B. Diffusion coefficients of sulfate and methane in marine sediments: Influence of porosity. *Geochim. Cosmochim. Acta* **1993**, *57*, 571–578, doi:10.1016/0016-7037(93)90368-7.
18. Boudreau, B.P. The diffusive tortuosity of fine-grained unlithified sediments. *Geochim.*

Cosmochim. Acta **1996**, *60*, 3139–3142, doi:10.1016/0016-7037(96)00158-5.
19. Ahmadi, M.M.; Mohammadi, S.; Hayati, A.N. Analytical derivation of tortuosity and permeability of monosized spheres: A volume averaging approach. *Phys. Rev. E - Stat. Nonlinear, Soft Matter Phys.* **2011**, *83*, doi:10.1103/PhysRevE.83.026312.
20. Larson, R.G.; Scriven, L.E.; Davis, H.T. Percolation theory of two phase flow in porous media. *Chem. Eng. Sci.* **1981**, *36*, 57–73, doi:10.1016/0009-2509(81)80048-6.
21. Dias, M.M.; Payatakes, A.C. Network models for two-phase flow in porous media Part 1. Immiscible microdisplacement of non-wetting fluids. *J. Fluid Mech.* **1986**, *164*, 337–358, doi:10.1017/S0022112086002586.
22. Thomson, P.R.; Jefferd, M.; Clark, B.L.; Chiarella, D.; Mitchell, T.M.; Hier-Majumder, S. Pore network analysis of Brae Formation sandstone, North Sea. *Mar. Pet. Geol.* **2020**, *122*, 104614, doi:10.1016/j.marpetgeo.2020.104614.
23. Blunt, M.J.; Bijeljic, B.; Dong, H.; Gharbi, O.; Iglauer, S.; Mostaghimi, P.; Paluszny, A.; Pentland, C. Pore-scale imaging and modelling. *Adv. Water Resour.* **2013**, *51*, 197–216, doi:10.1016/j.advwatres.2012.03.003.
24. Rabbani, A.; Mostaghimi, P.; Armstrong, R.T. Pore network extraction using geometrical domain decomposition. *Adv. Water Resour.* **2019**, *123*, 70–83, doi:10.1016/j.advwatres.2018.11.003.
25. Bultreys, T.; Van Hoorebeke, L.; Cnudde, V. Multi-scale, micro-computed tomography-based pore network models to simulate drainage in heterogeneous rocks. *Adv. Water Resour.* **2015**, *78*, 36–49, doi:10.1016/j.advwatres.2015.02.003.
26. Cai, J.; Lin, D.; Singh, H.; Wei, W.; Zhou, S. Shale gas transport model in 3D fractal porous media with variable pore sizes. *Mar. Pet. Geol.* **2018**, *98*, 437–447, doi:10.1016/j.marpetgeo.2018.08.040.
27. Gostick, J.; Aghighi, M.; Hinebaugh, J.; Tranter, T.; Hoeh, M.A.; Day, H.; Spellacy, B.; Sharqawy, M.H.; Bazylak, A.; Burns, A.; et al. OpenPNM: A Pore Network Modeling Package. *Comput. Sci. Eng.* **2016**, *18*, 60–74, doi:10.1109/MCSE.2016.49.
28. Johnson, T.F.; Levison, P.R.; Shearing, P.R.; Bracewell, D.G. X-ray computed tomography of packed bed chromatography columns for three dimensional imaging and analysis. *J. Chromatogr. A* **2017**, *1487*, 108–115, doi:10.1016/j.chroma.2017.01.013.
29. Zhang, L.; Chen, S.; Zhang, C.; Fang, X.; Li, S. The characterization of bituminous coal microstructure and permeability by liquid nitrogen fracturing based on μCT technology. *Fuel* **2020**, *262*, 116635, doi:10.1016/j.fuel.2019.116635.
30. Cooper, S.J.; Bertei, A.; Shearing, P.R.; Kilner, J.A.; Brandon, N.P. TauFactor: An open-source application for calculating tortuosity factors from tomographic data. *SoftwareX* **2016**, *5*, 203–210, doi:10.1016/j.softx.2016.09.002.
31. Al-Raoush, R.I.; Madhoun, I.T. TORT3D: A MATLAB code to compute geometric tortuosity from 3D images of unconsolidated porous media. *Powder Technol.* **2017**, *320*, 99–107, doi:10.1016/j.powtec.2017.06.066.
32. Phounglamcheik, A.; Bäckebo, M.; Robinson, R.; Umeki, K. The significance of intraparticle and interparticle diffusion during CO2 gasification of biomass char in a packed bed. *Fuel* **2022**, *310*, doi:10.1016/j.fuel.2021.122302.
33. Ramandi, H.L.; Mostaghimi, P.; Armstrong, R.T.; Saadatfar, M.; Pinczewski, W.V. Porosity and permeability characterization of coal: A micro-computed tomography study. *Int. J. Coal Geol.* **2016**, *154–155*, 57–68, doi:10.1016/j.coal.2015.10.001.